iScience

CellPress
OPEN ACCESS

Article

Leaflet-heterostructures by MWCNT self-assembly following electrospinning

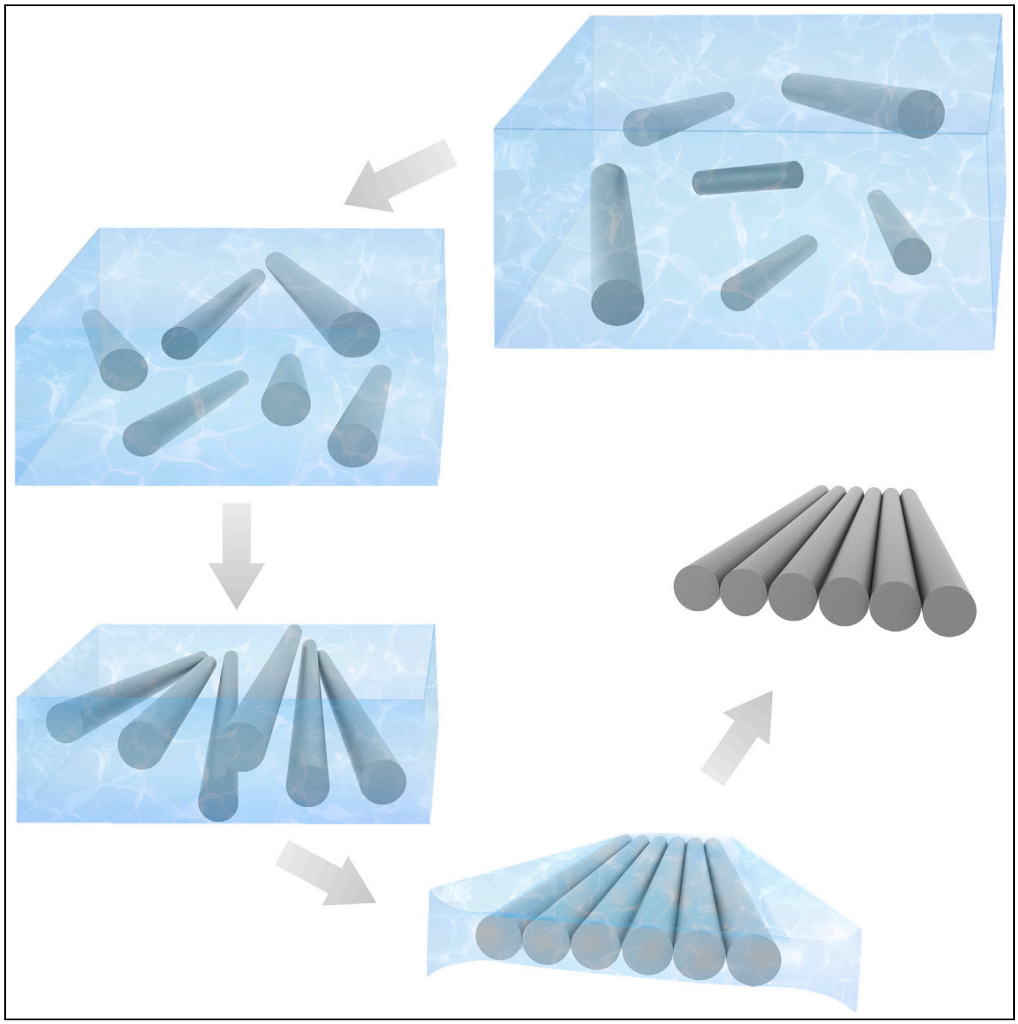

John Texter, Qi Li, Feng Yan

jtexter@emich.edu

Highlights

Stabilization of aqueous/PVA suspensions of MWCNT

Capillary force driven self-assembly of MWCNT

Evolution of meso-networks by electrospinning as PVA/MWCNT weight ratio decreased

Meso-networks comprise 2D heterostructures composed of laterally aligned MWCNT

Texter et al., iScience *27*, 110186
July 19, 2024 © 2024 The Author(s). Published by Elsevier Inc.
https://doi.org/10.1016/j.isci.2024.110186

iScience

CellPress
OPEN ACCESS

Article

Leaflet-heterostructures by MWCNT self-assembly following electrospinning

John Texter,[1,2,5,*] Qi Li,[3,4] and Feng Yan[3]

SUMMARY

Electrospinning of nanocarbons such as graphene and carbon nanotubes typically produces mats composed of one-dimensional fibers where the carrier polymer encapsulates the nanocarbons. Recently it was found that decreasing the amount of carrier polymer in approaching the electrospinning-electrospray boundary for graphene suspensions resulted in retention of the graphene two-dimensional anisotropy with one-dimensional carrier polymer fibers connecting flakes. We explored a similar decrease in carrier polymer in MWCNT suspensions to investigate the network topology that might ensue. Unexpectedly, two-dimensional leaflet meso-networks were obtained wherein the leaflets comprise laterally aligned MWCNTs one to several nanotubes thick. A mechanism based on capillary force-driven MWCNT self-assembly activated by menisci formed during drying of electrospun fibers is presented. Such materials offer new approaches to producing high surface-area coatings for catalytic and energy applications and suggest ways of formulating two-dimensional MWCNT assemblies in metal foams and other open-cell porous materials.

INTRODUCTION

2D networks in catalysis and energy

Two-dimensional (2D) materials and networks are becoming increasingly important in designing advanced catalytic electrodes and membranes for energy storage and conversion,[1–3] and they offer novel and diverse design opportunities for multifunctional catalytic systems. Heterostructures derived from 2D materials provide independent approaches to tuning electronic structure, an important feature in modifying catalytic activity[4,5] and an important new tool for interfacial engineering.[2] Such heterostructures include sandwich core-shell structures of one type of nanosheet (MoS_2) encapsulated in another (heavily pyrrolic N doped graphene),[6] Ni/Fe layered double hydroxides (LDH) sheets interspersed with MoS_2 nanosheets,[7] phosphorene/graphene bilayers,[8] reduced graphene oxide (rGO) – graphitic carbon nitride nanostructures,[9] alternating graphitic boron-nitride and MoS_2 nanosheets,[10] and electrically conducting 1T-MoS_2 domains within 1H-MoS_2 nanosheets,[11] among numerous other examples. Another important class of heterostructures are graphene foams and related porous materials for catalysis,[11,12] EMI shielding,[13,14] electrical double layer capacitors,[15,16] microwave absorbers,[17,18] electrodes for batteries[19–21] and solar cells,[22] and other applications ranging from oil-water separation[23] to sensors.[24] In each case, a basic building block of the respective heterostructure is a flake of a 2D material that very often is a graphene flake.

Electrospinning of MWCNT

Electrospinning[25,26] is becoming increasingly studied to create non-woven mats for diverse applications and membranes, and the main product is typically a one-dimensional (1D) very thin fiber composed of a desired polymer. It is common to create nanocomposite fibers[25,27] by simply spinning suspensions of particles in the presence of an appropriate carrier polymer such as PVP (polyvinylpyrrolidone) or PVA (polyvinyl alcohol). There have been many reports of e-spinning MWCNTs,[28–35] and the MWCNTs are typically embedded in the carrier polymer, yielding 1D fibers similar to control fibers obtained without MWCNTs. No previous report of electrospinning MWCNTs has reported generation of 2D structures. Similarly, in the electrospinning of graphene suspensions, the graphene flakes typically are "rolled up" within the electrospun fibers.[36] However, one of our reports showed how the 2D anisotropy of graphene flakes could be realized in fibers by sufficiently decreasing the carrier polymer to graphene weight ratio.[37] In this report we find that 2D leaflet heterostructures form when the carrier polymer to MWCNT weight ratio becomes sufficiently small.

[1]Strider Research Corporation, Rochester, NY 14610-2246, USA
[2]Coating Research Institute, School of Engineering, Eastern Michigan University, Ypsilanti, MI 48197, USA
[3]Department of Polymer Science and Engineering, College of Chemistry, Chemical Engineering and Materials Science, Soochow University, Suzhou 215123, China
[4]Present address: College of Chemistry and Chemical Engineering, Nantong University, Nantong 226019, China
[5]Lead contact
*Correspondence: jtexter@emich.edu
https://doi.org/10.1016/j.isci.2024.110186

This is an open access article under the CC BY-NC-ND license (http://creativecommons.org/licenses/by-nc-nd/4.0/).

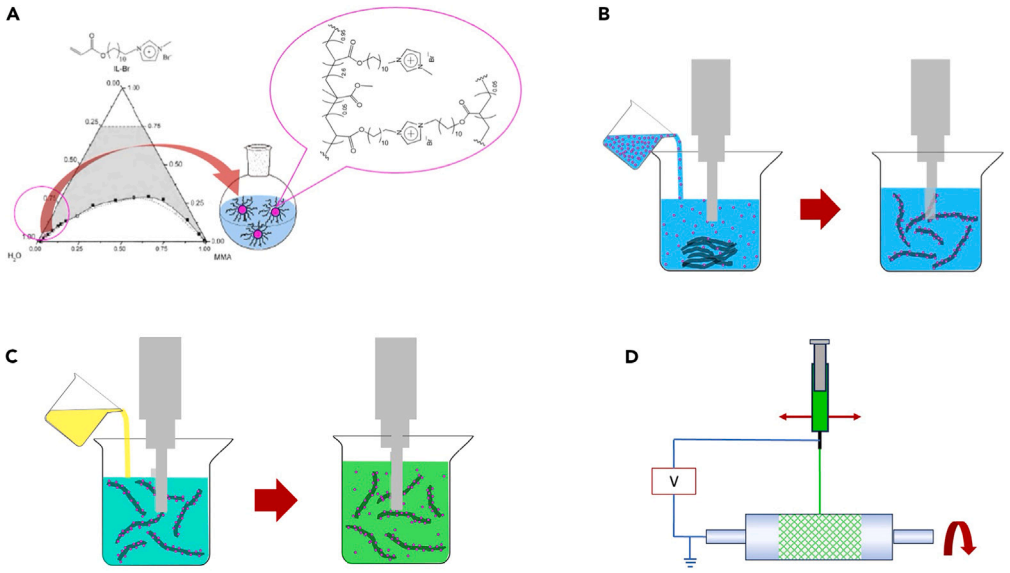

Figure 1. Dispersion preparation and electrospinning

Schematic of (A) synthesis of lightly crosslinked co-polymerized ionic liquid with methylmethacrylate using microemulsion polymerization to produce 20–30 nm diameter nanolatexes, NLs.

(B) Admixture of aqueous suspension of NLs with aggregates of MWCNT in water followed by sonication to yield stable aqueous dispersion of NL-stabilized MWCNT.

(C) Admixture of aqueous polyvinyl alcohol (PVA) solution with NL-stabilized MWCNT suspension driven by mild sonication.

(D) High-voltage, V, of 20 kV drives electrospinning of an aqueous PVA suspension of NL-stabilized MWCNT onto an aluminum foil target on a rotating drum; the dispensing needle is rastered back and forth to produce an approximately 8–10 cm wide coating on the rotating target.

Overview

The production of nonwoven MWCNT mats on an aluminum-foil rotating target is illustrated in Figure 1 as a four-step process. First, a stabilizer that provides thermodynamically stable dispersions in water of MWCNTs is prepared. In this study, we used a polymerized ionic liquid,[38–40] a nanolatex (NL) stabilizer based on an ionic liquid monomer, ILBr,[41–44] co-polymerized with methyl methacrylate, MMA. This NL stabilizer, lightly cross-linked due to alkyl scrambling during ILBr synthesis to produce N,N-bis[1-(2-acryloyloxyundecyl)]imidazolium bromide as a minor side product,[45,46] was synthesized by microemulsion polymerization[41–44] (Figure 1A) and has been used to produce aqueous MWCNT dispersions at up to 17% by weight MWCNT.[47,48] It has also been found very useful for dispersing SWCNT,[49] hydrothermal carbons,[50] and graphene[51] (at up to 6.4% graphene by weight) in water. The "active" moiety in this NL is the imidazolium bromide functional group that provides two important functions: (1) strong binding to the MWCNT sp^2 surface via π-π orbital overlap between filled imidazolium π orbitals and half-empty π orbitals on MWCNT surfaces; (2) strong aqueous hydration of imidazolium bromide ion-pairs by water. This "bifunctionality" (dual efficacy) bridges the hydrophobic surface energy of sp^2 surfaces and the relatively high surface energy of water, thereby yielding thermodynamically stable dispersions. It is noteworthy that aqueous nanocarbon dispersions can reliably be made using a variety of imidazolium-based polymerized ionic liquids.[52]

The production of such aqueous MWCNT dispersions is illustrated in Figure 1B using a lab-scale ultrasonic device. MWCNT (Baytubes)[53–55] were obtained as a gift from Bayer MaterialsScience. These MWCNTs were reported to average 13–16 nm[55] in diameter and 1 μm to more than 10 μm[51] in length before sonication. Our own SEM measurements[45] have indicated they are 30–50 nm in diameter. Sonication (5 min) in ethanol cut such tubes to lengths of 200–1000 nm.[55] Baytubes were provided as black powder aggregates 300–1000 μm in diameter, and we used these aggregates to produce stable aqueous dispersions by ultrasonicating crude suspensions of such powder aggregates in aqueous nanolatex dispersions.

The third step, Figure 1C, is addition of the carrier polymer, polyvinyl alcohol (PVA), to the aqueous MWCNT suspension. Mixing is facilitated by using sonication. The fourth step in producing our coatings is electrospinning of the PVA/MWCNT suspension produced in step 3. We used an electrospinning system with an aluminum foil target wrapped around a rotating mandrel (drum) and a needle assembly that was rastered back and forth during operation.

Our NL was prepared using AIBN (azobisisobutyronitrile) thermal initiation at 60°C by microemulsion polymerization as mentioned above. The diameters of the NL were in the range of 20–30 nm as determined by dynamic light scattering. Our aqueous MWCNT dispersion, about 10 g, was prepared at 4.8% by weight MWCNT and 2.4% NL. A pre-dispersion with all components was activated for 15 min in an ultrasonic cleaning bath (Branson Model B300, Danbury, CT, USA), and then further activated using a micro-tip sonic horn about 4 mm in diameter at the tip end (SONIS Vibra-Cell, Model VC 30, Newtown, CT, USA)[51] Sonic horn treatment was done by suspending the reactor (vial) in an ice-water bath with the horn tip about 1 cm above the bottom of the reactor vial. Sonication was done for about 8 h.

Dilutions of the above-described MWCNT/NL dispersion were used to prepare suspensions for electrospinning. The carrier polymer, PVA, had a nominal number-average molecular weight of about 80 kDa and a degree of polymerization, DP, of about 1750. This DP corresponds to a linear length of about 380 nm. Suspensions for spinning were sonicated for 30 min to form a stable suspension prior to electrospinning.

Electrospinning was done using a system that was obtained from Foshan Lepton Precision Measurement and Control Technology Co. Ltd. (model QENZ-E05, Foshan, China). A potential of about 20 kV was used to polarize the electrospinning suspension, and the 22-gauge-steel needle tip was about 10 cm away from the aluminum foil target fixed to a rotating mandrel. The aqueous MWCNT/NL-PVA suspension was fed to the needle by a 10 mL syringe pump at a flow rate of 0.6 mL h^{-1}. The needle was rastered back and forth over a distance of about 10 cm to produce a coating on the rotating target about 10 cm wide. The target and drum were rotated at about 400 revolutions per minute. The as-spun fibrous films were dried overnight in a vacuum at room temperature to remove weakly bound water.

RESULTS

The nonwoven-mat topologies obtained as a function of PVA:MWCNT weight ratio are illustrated in Figure 2. The PVA control mat (web), Figure 2A, shows that there is some 2D character to the PVA fibers obtained in the absence of MWCNT suspension. The mat obtained by adding PVA in large excess, at a PVA to MWCNT weight ratio of 6:1 is illustrated in Figure 2B, and only two differences with the PVA control are evident: (1) The impact of nanolatex-stabilized MWCNT induces small-amplitude irregularities (undulations) along the fiber edges. (2) There are a small number of apparent "bulging" structures along some of the fibers (highlighted with green-dashed circles). These structures may be precursors to 2D leaflet formation, but at this point are not primary objects of this study. Figure 2C, at a PVA to MWCNT ratio of 4:1 and at higher magnification than in Figures 2A and 2B, illustrates (3) increased longitudinal undulations of the fibers and (4) an apparent onset of fiber bifurcation, highlighted by magenta dotted-circles. We have not attempted to highlight all of these bifurcations because of the limited depth of field available and because some cannot be easily distinguished from overlapping fibers. We believe that these bifurcations represent the onset of meso-network formation and are discussed further below.

The mat of Figure 2D obtained with a PVA to MWCNT ratio of 2:1 also illustrates structures seen in Figures 2B and 2C. Similar structures are also highlighted within green and magenta circles, respectively, in Figure 2D. Two "leaflet" structures are highlighted with cyan oval shapes and appear to be examples where bifurcations of the type highlighted within magenta circles grow in width. Also, the basic widths of fibers evident in Figure 2C appear to narrow in Figure 2D, where the PVA to MWCNT weight ratio drops 50% from 4:1 to 2:1. Further dramatic narrowing of fibers is seen in Figures 2E and 2F, where the PVA to MWCNT weight ratio drops further to 1:1 and 0.5:1, respectively. Concomitantly, we see meso-network formation of apparent 2D leaflets, wherein leaflets and meso-networks are interconnected by narrow fibers. These meso-networks are the main features we wish to discuss. The MWCNTs in their aqueous dispersion are stabilized by nanolatexes, NLs, at an MWCNT to NL weight ratio of 1:0.5, and this ratio is constant in each mat containing MWCNTs.

We term these structures meso-networks because they appear somewhat clustered rather than as individually isolated 2D films or membranes. Closer inspection of such networks is illustrated in Figures 3 and 4 for 0.5:1 PVA:MWCNT. The magnification series in Figure 3 suggests MWCNTs, coated with NLs, provide a somewhat random network supporting such membranes. Between and on MWCNT and NLs we presume there are PVA film regions serving a binder function.

DISCUSSION

The apparent 2D leaflet structures seen in Figures 2E and 2F are reminiscent of the PVA, graphene, and nanolatex networks created by the same electrospinning process wherein graphene flakes were also stabilized by nanolatexes 20–30 nm in diameter.[37] A key aspect of graphene flakes is that they are quintessential 2D materials. However, here there were no 2D materials used in formulating the suspensions used in our electrospinning processing. Our further analysis is based on "drilling down" the SEM of Figure 3A for the 0.5:1 PVA:MWCNT coating. We focus on regions associated with the meso-network illustrated in Figure 2F. The approximately 60 μm × 50 μm field illustrated in Figure 3A shows that the coating is not dense in meso-networks (clusters). Such clusters are interspersed among relatively sparsely coated regions.

Analysis of SEM images

Figure 3B illustrates approximately 6–10 meso-networks, and we highlight a rectangular region therein from the top-central portion of Figure 2F that is further magnified in Figure 3C. The image of Figure 3D illustrates that partially isolated fibers are defined by segments of MWCNT. Also evident at various places in Figure 3 are isolated single, linear chains. The NL mass is about the same as that of the PVA, and each is half the MWCNT mass. The PVA strands cannot be resolved, but their distribution is the primary reason individual MWCNT cannot more easily be resolved. Further, the 2D leaflet character structurally is more complex than arising from a PVA membrane formed by drying menisci supported by MWCNT networks.

Figure 4A overlaps with Figure 3D, and two approximately 0.25 μm^2 areas magnified in Figures 4B and 4C reveal significant structural aspects of the 2D leaflets. The major result is that the 2D layers are composed of densely packed MWCNT. Also visible in Figures 4B and 4C are linear arrays of NLs on some of the MWCNTs that make it easier to visualize the underlying MWCNTS and their packing relative to proximal MWCNTs. These images in Figures 4B and 4C are displayed in Figure 5 at increasing levels of contrast to help delineate the interfaces between the MWCNTs and to highlight the NLs.

The wider field images in Figure 3 show that these leaflet structures are 2D in nature, though some of them exhibit flower-petal-like curvature, such as shown in Figure 3D. The depth of field of SEM makes clear, however, that these leaflets are not necessarily one

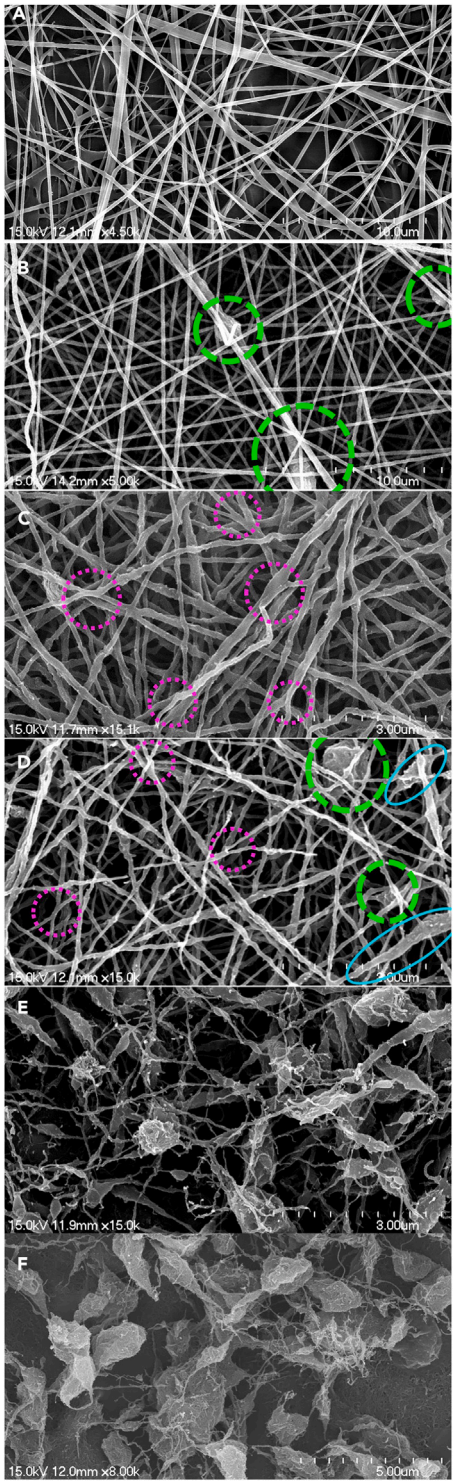

Figure 2. Development of meso-networks as carrier polymer decreased

SEM of electrospun coatings with decreasing PVA/MWCNT weight ratios: (A) 1: 0 (PVA control), 10 μm scale marked in 1 μm increments.
(B) 6:1, 6 μm of scale marked in 1 μm increments.
(C) 4:1, 3 μm scale marked in 300 nm increments.
(D) 2:1, 3 μm scale marked in 300 nm increments.
(E) 1:1, 3 μm scale marked in 300 nm increments.
(F) 0.5:1, 5 μm scale marked in 500 nm increments. The features highlighted with green, magenta, and cyan are discussed further in the text.

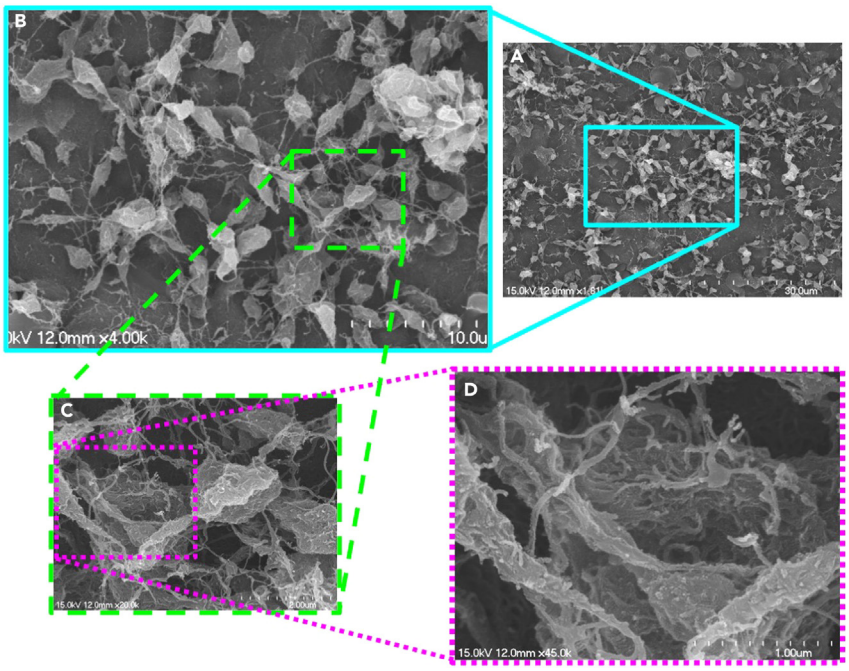

Figure 3. Leaflet heterostructures in meso-networks

SEM of PVA:MWCNT 0.5:1 coating illustrating meso-network structural and compositional aspects.

(A) Portion of coating on aluminum foil target, 30 μm scale marked in 3 μm increments.

(B) Cyan-rectangular region of (A) magnified 3x illustrating clusters of 2D meso-network leaflets, 7 μm of scale marked in 1 μm increments.

(C) Green-dashed region of (B) magnified ~2x illustrating meso-network cluster, 2 μm scale marked in 200 nm increments.

(D) Magenta-dotted region of (C) magnified ~2.5x illustrating multi-leaflet region of meso-network, 1 μm scale marked in 100 nm increments.

MWCNT thick, and the contrast series shows tiered layering suggesting thicknesses of at least two and three MWCNTs (and more are quite feasible).

The contrast series of Figure 5 highlights important features of the MWCNT packing. The main feature is that individual layers appear dense in MWCNT. The MWCNTs are aligned side by side, but not in a longitudinally very extended way as they might be if polarized by an electric field. The cartoon illustrating this association in the article graphic was composed to accentuate capillary force assembly discussed below. Various geometric patterns are evident in this sampling. Also, vacancy-type defects in this dense packing are also evident. Areal type "vacancies" are shown in the top images of Figure 5, where occluded areas appear to be barred from further space-filling or are simply empty. Also, small spaces between aligned MWCNT are visible, and we call attention to the concentrically oval alignment illustrated in the lower right quadrant of the bottom images of Figure 5.

Figure 5 also serves to show how the NLs adsorbed to MWCNT help to clarify the geometry of the underlying MWCNT packing. While it is known that such NLs in water at concentrations greater than 25% by weight can form a gel phase, other studies have shown their binding to MWCNTs is slowly reversible. Here, the dense packing shows that MWCNTs that are aligned with one another must induce NL desorption in order to benefit from van der Waals close packing.

A significant contributor to these phenomena is the cutting of the MWCNT during the sonication of the parent aqueous MWCNT/NL dispersion and during the admixture of this dispersion with aqueous PVA to make the aqueous suspension processed by electrospinning. Examination of SEM of a PVA-MWCNT-NL suspension showtes that the MWCNT lengths vary between 200 nm and 800 nm in length. These lengths are consistent with the packing seen in Figure 5, though packing of an MWCNT segment partially in one layer and extending into an adjacent layer cannot be discounted.

Lastly, the PVA is present at half the mass level of the MWCNT and the same mass level of the NLs, but these are inherently small 1D objects with a nominal number-average molecular weight of about 80 kDa and projected linear lengths of about 380 nm with a degree of polymerization of about 1750. As a random coil, very dilute random coils would have a radius of gyration of about 110 nm ($b[N/6]^{1/2}$; $b \approx 6.5$). Intramolecular hydrogen bonding likely produces solution spheroidal structures having radii smaller than 110 nm, but nevertheless, we expect them to be of low density and difficult to image as colloidal objects. When dried, the PVA contributes to film formation.

Mechanism of meso-network membrane formation

The meso-2D networks illustrated comprise four chemical components: PVA, NL, MWCNT, and water of hydration. During electrospinning and the ensuing drying, three phases support the formation of these networks. The NL constitutes a nanophase because they are a lightly

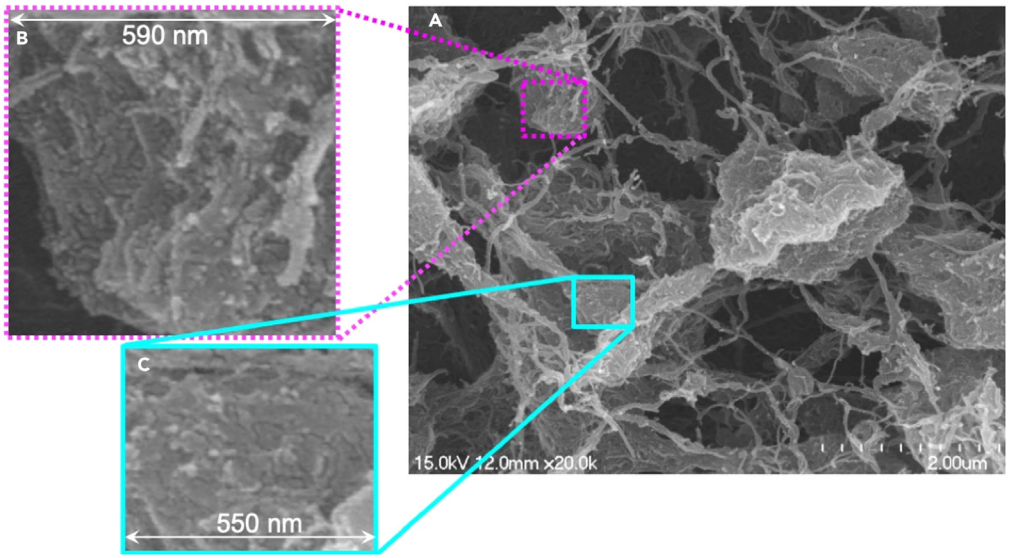

Figure 4. Examination of MWCNT packing in meso-network

Magnified (A) view of SEM of PVA:MWCNT 0.5:1 coating from Figure 3C illustrating (B) and (C) micro- and nano-structural compositional aspects including alignment of MWCNTs and decoration of MWCNT with nanolatexes. In (A) the 2 μm scale is marked in 200 nm increments.

cross-linked hydrogel, and the MWCNTs compose an allotrope of carbon. The way these phases separate from aqueous suspension and assemble to generate the 2D leaflet structures of Figures 2E and 2F highlights key colloidal phenomena.

The low magnification SEM of Figures 3A and 3B show that the coatings are not dense in meso-networks, and this varied density distinguishes these coatings from the PVA control coatings exemplified by the SEM of Figure 2A, typical of non-woven mats obtained by electrospinning with rastering. No doubt, these differences are due in part to the rastering used to coat the rotating target. The contrast between Figures 2A and 2F underscores the existence of significant topological differences in the drying of our electrospun multiphase suspensions, particularly because there were only 0D and 1D components in our suspensions, although 2D heterostructured meso-network coatings are obtained. An important starting point for our mechanistic discussion is that each meso-network illustrated comprises a 3D network of fibers, thereby articulating a 3D foam. Such "foams" form natural supports for multiple menisci, and we assert that the leaflet structures illustrated are the dried products of such menisci.

The above image analysis provides some insight because we see that leaflet structures are inherently dense in segmentally aligned MWCNT. However, we are still left with trying to rationalize how a suspension of MWCNT could form such leaflet structures. Random aggregation would be expected to produce 3D aggregates rather than the meso-networks observed. In our present system, we have a transformation from cylindrical symmetry to 2D on drying. We want to understand what forces direct 2D arrangements of the MWCNT. The fibers connecting meso-networks and leaflets within such networks appear to be composed mainly of MWCNT, NL, and PVA.

It is important to understand if an association of nanorods might have provided some expectation of this MWCNT association. Of about 800 papers that address nanorods and electrospinning, only 103 (listed in Table S1 referenced in the SI) topically mention membranes. None of these discuss any formation of 2D structures emanating from assemblies of nanorods.

Rationalizing precipitation, solidification, and crystallization processes in terms of van der Waals, polar, electrostatic, and H-bonding interactions is a standard approach. Here in this meso-network system exhibiting novel supramolecular assembly aspects, our discussions are of forces and interactions that are magnified and longer range. We suggest that these 2D leaflet structures form in response to two nanoscale self-association forces: (1) bead (NL) and rod (MWCNT) necklace formation threaded by PVA strands forming H-bonds, polar bonds, and dispersion force bonds with NL (polymerized ionic liquid) segents and groups; (2) capillary force-driven associations during drying that bring MWCNTs coated with NL into closely aligned association.

Bead-necklace model of MWCNT association

Cabane and Duplessix[56] explained how polymers, often poly-electrolytes, tied spherical and cylindrical micelles together to form micellar networks. Such networks became known as the bead-necklace model. Similarly, the formation of analogous networks wherein polymer chains tied together particles became appreciated as a mechanism for forming loose flocs of particles.[57] The nominal 380 nm lengths of our PVA chains appear sufficiently long to tie proximal MWCNTs together in suspension. Bare MWCNT sp^2 surfaces are inherently hydrophobic, but when coated with NL they are compatible with water. The ester and imidazolium groups of these NLs provide multiple sites for hydrogen bonding and polar interactions with PVA, particularly with the hydroxyl groups of PVA, and these interactions likely become stronger as drying proceeds in these electrospun coatings. Thus, one can see how PVA anchoring to two or more NLs on separate MWCNTs can establish loose links between proximal MWCNTs that help maintain the proximity of such MWCNTs to one another during drying and, subsequently, further

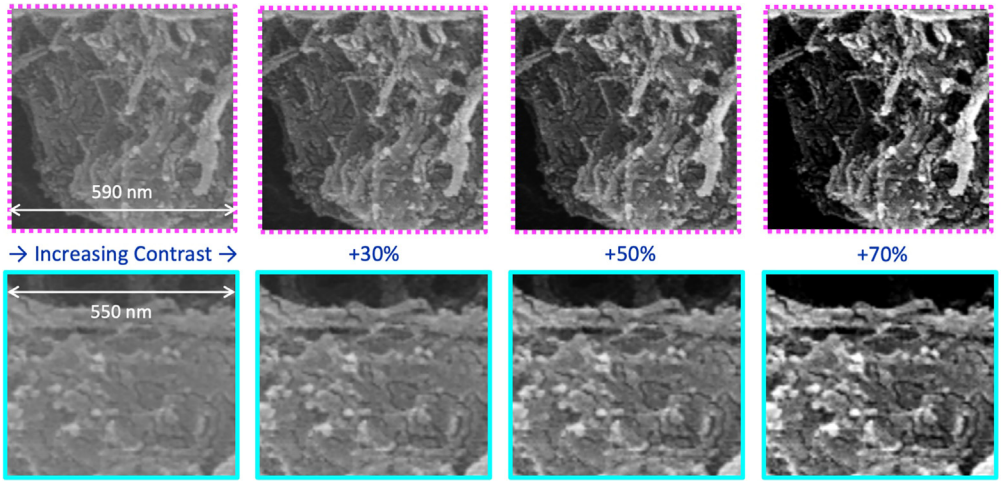

Figure 5. Impact of contrast variations on discerning MWCNT packing

Effects of increasing contrast (+30%, +50%, and +70%) on Figures 4B (top) and 4C (bottom).

association. Therefore, PVA chains provide connectivity and binding between NLs and MWCNTs. This connectivity is important in leaflets and in inter-network and intra-network fiber formation.

The most well-known 2D materials such as graphene, h-C_2N_2, and MoS_2, among many others, rely on dispersion forces to hold nanosheets to one another. In almost all 2D materials, inorganic and organic, dispersion forces are significant contributors to intersheet attraction. We have not found any reports that apply the bead-necklace model to drive association of 2D nanosheets.

SEM of the 2D leaflets derived from MWCNTs bear great similarity to graphene coatings made by electrospinning. Compare Figure 3B with Figures SI-S5 obtained for graphene electrospinning. They are difficult to distinguish. In general, however, 2D materials of inorganic composition exhibit rigid planar structures, while the leaflets we report exhibit diverse curvatures.

Capillary forces during drying

2D arrays of monodisperse spherical nanoparticles can be obtained by a process of drying that has become known as the coffee ring effect.[58,59] This phenomenon requires a supporting substrate and is driven by capillary forces that have been explored in hundreds of publications.[59–61] The strongest interparticle capillary forces come into play when a liquid bridge (meniscus or lens) connects the particles. These capillary forces operate during the drying of films on substrates (coffee ring effect). They also operate during the thinning of films and the formation of menisci.[62] The MWCNTs ultimately are attached to both sides of a meniscus and become subject to capillary forces. These forces have been discussed quantitatively by Kratchelvsky et al.[63,64] The 2D arrangement of assembled MWCNTs appears assignable in part to the 2D nature of the menisci that form during drying.

Transitioning from high levels of carrier polymer to low levels produces 2D heterostructures comprising meso-networks of leaflets and interconnecting fibers. The leaflet structures appear to comprise aligned and layered MWCNTs. This alignment is tentatively assigned to inter-MWCNT capillary forces that come into play during the late stages of menisci drying.

Further characterizations

While the depth of field provided by SEM in Figures 3 and 4 provides significant morphological characterizations of these electrospun coatings, a variety of other physical properties, such as mechanical durability, electrical conductivity, and capacitance (charge storage), are of keen interest. The coatings reported here on aluminum supports (and current collectors) cannot be separated from the support without being structurally destroyed. Therefore, mechanical measurements are not yet feasible. We think broadband dielectric spectroscopy measurements of electrical conductivity, however, may be feasible with appropriate spacers in a sandwich geometry.[65,66] The feasibility of making analogous coatings on dissolvable collector materials (e.g., alumina/silica cloth) is also under investigation, and if successful, it may be possible to pursue mechanical, electrical, and optical measurements on free-standing electrospun coatings.

Applications

We believe that the most useful applications of these electrospun meso-networks will be in stimulating the design of derivative materials for specific applications. Several other derivative materials and associated potential applications are outlined in the SI because of the intrinsic speculation involved. An implicit utility of these electrospun meso-networks is the extent to which they are stimulating further applications of the bead-necklace model and of capillary forces generated during the drying of complex fluids. We expect that such multiphase

suspensions as used herein may provide simple means (immersion and drying) to construct 2D films in inter-pore windows between pores in open-cell porous materials and metal foams.

Summary and outlook

This study shows that a profound change in coating morphology occurs as the weight fraction of carrier polymer (PVA) is decreased. Concomitantly, we observe the formation of meso-networks of 2D leaflets. This leaflet formation represents the spontaneous formation of a *new class* of 2D materials composed of aligned MWCNTs. Future work to verify or refute the mechanistic importance of bead-necklace connections and capillary forces in forming layered leaflet structures dense in MWCNTs is needed, as are more extensive characterizations of mechanical, electrical, and optical properties.

We believe that the most useful applications of these electrospun meso-networks will be in stimulating the design of derivative materials for specific applications. Several other derivative materials and associated potential applications are outlined in the supplemental information because of the intrinsic speculation involved. An implicit utility of these electrospun meso-networks is the extent to which they may stimulate further scientific examinations and applications of the bead-necklace model and of capillary forces generated during the drying of complex fluids wherein both sides of menisci are exposed to ambient vapor.

If the electrical conductivity of such coatings is sufficient, or if it can be made to be sufficient, such electrospinning may offer practical (high volume) means to create electrodes competitive with graphene foams that offer dramatically higher specific surface area per cm^2 than can be obtained from a conformal coating.

Limitations of the study

The toughness and brittleness of our electrospun coatings are unknown, and we are not yet sure how to effectively measure these properties with aluminum foil as the collector. In an upcoming project, we will investigate the use of alumina/silica (ASC) cloth as a collector. We will impregnate the ASC with metal nanoparticles and metal coatings in case the ASC prevents sufficient electrical polarization during electrospinning. If electrospinning is successful, the ASC coatings will be dissolved in weak aqueous base. This will generate "coatings" free of substrate (aluminum foil collector) for mechanical, electrical, and optical characterization.

The electrical conductivity of such coatings should be measurable by dielectric spectroscopy methods discussed above for nanoparticle SnO_2 and conducting polymer latex coatings. We expect such coatings to exhibit ionic conductivity because the nanofibers connecting 2D leaflets are composed of nanolatex and PVA, and the 2D leaflets are coated with nanolatex.

STAR★METHODS

Detailed methods are provided in the online version of this paper and include the following:

- KEY RESOURCES TABLE
- RESOURCE AVAILABILITY
  - Lead contact
  - Materials availability
  - Data and code availability
- METHOD DETAILS
  - Synthesis of ionic liquid acrylate monomer, ILBr
  - Synthesis of nanolatex
  - Structural properties
  - Electrospinning

SUPPLEMENTAL INFORMATION

Supplemental information can be found online at https://doi.org/10.1016/j.isci.2024.110186.

ACKNOWLEDGMENTS

Q.L. gratefully acknowledges financial support from the Natural Science Foundation of Jiangsu Province (BK20210834). J.T. thanks F.Y. and the School of Chemistry, Chemical Engineering, and Materials Science, Soochow University, for their hospitality during his 2019 visit. Financial support from the United States Air Force Office of Scientific Research Grant No. FA9550-08-1-0431 is also gratefully acknowledged. The assistance of Dr. Yin Hu in composing the graphic for this paper is gratefully acknowledged.

AUTHOR CONTRIBUTIONS

J.T. conceived the project and provided the aqueous nanolatex-stabilized MWCNT dispersions, and Q.L. executed the electrospinning and characterization experiments. F.Y. provided the electrospinning and characterization facilities. J.T., Q.L., and F.Y. contributed to writing and revising the manuscript.

DECLARATION OF INTERESTS

J.T. and F.Y. acknowledge having equity interests in US Patent 7,759,401, and J.T. acknowledges his equity interest in US Patent 8,920,682. Both patents are assigned to Eastern Michigan University.

Received: September 27, 2023
Revised: April 1, 2024
Accepted: June 3, 2024
Published: June 6, 2024

REFERENCES

1. Tao, H., Gao, Y., Talreja, N., Guo, F., Texter, J., Yan, C., and Sun, Z. (2017a). Two-dimensional nanosheets for electrocatalysis in energy generation and conversion. J. Mater. Chem. A *5*, 7257–7284. https://doi.org/10.1039/c7ta00075h.
2. Sun, Z., Talreja, N., Tao, H., Texter, J., Muhler, M., Strunk, J., and Chen, J. (2018). Catalysis of carbon dioxide photoreduction on nanosheets: Fundamentals and challenges. Angew. Chem. Int. Ed. *57*, 7610–7627. https://doi.org/10.1002/anie.201710509.
3. Tao, H., Fan, Q., Ma, T., Liu, S., Gysling, H., Texter, J., Guo, F., and Sun, Z. (2020). Two-dimensional materials for energy conversion and storage. Prog. Mater. Sci. *111*, 100637. https://doi.org/10.1016/j.pmatsci.2020.100637.
4. Tao, H., Zhang, Y., Gao, Y., Sun, Z., Yan, C., and Texter, J. (2017b). Scalable exfoliation and dispersion of two-dimensional materials - an update. Phys. Chem. Chem. Phys. *19*, 921–960. https://doi.org/10.1039/C6CP06813H.
5. Xu, L., Iqbal, R., Wang, Y., Taimoor, S., Hao, L., Dong, R., Liu, K., Texter, J., and Sun, Z. (2024). Emerging two-dimensional materials: Synthesis, physical properties, and application for catalysis in energy conversion and storage. Innovat. Mater. *2*, 100060. https://doi.org/10.59717/j.xinn-mater.2024.100060.
6. Yuan, K., Zhuang, X., Fu, H., Brunklaus, G., Forster, M., Chen, Y., Feng, X., and Scherf, U. (2016). Two-dimensional core-shelled porous hybrids as highly efficient catalysts for the oxygen reduction reaction. Angew. Chem. Int. Ed. *55*, 6858–6863. https://doi.org/10.1002/anie.201600850.
7. Nayak, S., Swain, G., and Parida, K. (2019). Enhanced photocatalytic activities of RhB degradation and H_2 evolution from *in situ* formation of the electrostatic heterostructure MoS_2/NiFe LDH nanocomposite through the Z-scheme mechanism via p-n heterojunctions. ACS Appl. Mater. Interfaces *11*, 20923–20942. https://doi.org/10.1021/acsami.9b06511.
8. Guo, G.C., Wang, D., Wei, X.L., Zhang, Q., Liu, H., Lau, W.M., and Liu, L.M. (2015). First-principles study of phosphorene and graphene heterostructure as anode materials for rechargeable Li batteries. J. Phys. Chem. Lett. *6*, 5002–5008. https://doi.org/10.1021/acs.jpclett.5b02513.
9. Ong, W.-J., Tan, L.-L., Chai, S.-P., Yong, S.-T., and Mohamed, A.R. (2015). Surface charge modification via protonation of graphitic carbon nitride (g-C_3N_4) for electrostatic self-assembly construction of 2D/2D reduced graphene oxide (rGO)/g-C_3N_4 nanostructures toward enhanced photocatalytic reduction of carbon dioxide to methane. Nano Energy *13*, 757–770. https://doi.org/10.1016/j.nanoen.2015.03.014.
10. Thangasamy, P., Partheeban, T., Sudanthiramoorthy, S., and Sathish, M. (2017). Enhanced superhydrophobic performance of BN-MoS_2 heterostructure prepared via a rapid, one-pot supercritical fluid processing. Langmuir *33*, 6159–6166. https://doi.org/10.1021/acs.langmuir.7b00483.
11. Qi, Y., Xu, Q., Wang, Y., Yan, B., Ren, Y., and Chen, Z. (2016). CO_2-Induced phase engineering: Protocol for enhanced photoelectrocatalytic performance of 2D MoS_2 nanosheets. ACS Nano *10*, 2903–2909. https://doi.org/10.1021/acsnano.6b00001.
12. Song, X., Chen, Y., Rong, M., Xie, Z., Zhao, T., Wang, Y., Chen, X., and Wolfbeis, O.S. (2016). A phytic acid induced super-amphiphilic multifunctional 3D graphene-based foam. Angew. Chem. Int. Ed. *55*, 3936–3941. https://doi.org/10.1002/anie.201511064.
13. Shen, B., Li, Y., Yi, D., Zhai, W., Wei, X., and Zheng, W. (2016). Microcellular graphene foam for improved broadband electromagnetic interference shielding. Carbon *102*, 154–160. https://doi.org/10.1016/j.carbon.2016.02.040.
14. Zhang, S., Sun, H., Lan, T., Liu, X., and Ran, Q. (2021). High electromagnetic interference shielding effectiveness achieved by multiple internal reflection and absorption in polybenzoxazine/graphene foams. J. Appl. Polym. Sci. *138*, e51318. https://doi.org/10.1002/app.51318.
15. Yan, J., Ding, Y., Hu, C., Cheng, H., Chen, N., Feng, Z., Zhang, Z., and Qu, L. (2014). Preparation of multifunctional microchannel-network graphene foams. J. Mater. Chem. A *2*, 16786–16792. https://doi.org/10.1039/C4TA03057E.
16. Pan, Z., Liu, M., Yang, J., Qiu, Y., Li, W., Xu, Y., Zhang, X., and Zhang, Y. (2017). High electroactive material loading on a carbon nanotube@3D graphene aerogel for high-performance flexible all-solid-state asymmetric supercapacitors. Adv. Funct. Mater. *27*, 1701122. https://doi.org/10.1002/adfm.201701122.
17. Zhang, Y., Huang, Y., Zhang, T., Chang, H., Xiao, P., Chen, H., Huang, Z., and Chen, Y. (2015). Broadband and tunable high-performance microwave absorption of an ultralight and highly compressible graphene foam. Adv. Mater. *27*, 2049–2053. https://doi.org/10.1002/adma.201405788.
18. Shu, R., Xu, J., Wan, Z., and Cao, X. (2022). Synthesis of hierarchical porous nitrogen-doped reduced graphene oxide/zinc ferrite composite foams as ultrathin and broadband microwave absorbers. J. Colloid Interface Sci. *608*, 2994–3003. https://doi.org/10.1016/j.jcis.2021.11.030.
19. Xu, J., Wang, M., Wickramaratne, N.P., Jaroniec, M., Dou, S., and Dai, L. (2015). High-performance sodium ion batteries based on a 3D anode from nitrogen-doped graphene foams. Adv. Mater. *27*, 2042–2048. https://doi.org/10.1002/adma.201405370.
20. Wang, B., Li, S., Wu, X., Liu, J., and Tian, W. (2016). Hierarchical $NiMoO_4$ nanowire arrays supported on macroporous graphene foam as binder-free 3D anodes for high-performance lithium storage. Phys. Chem. Chem. Phys. *18*, 908–915. https://doi.org/10.1039/c5cp04820f.
21. Yao, Y., Zhu, Y., Huang, J., Shen, J., and Li, C. (2018). Porous CoS nanosheets coated by N and S doped carbon shell on graphene foams for free-standing and flexible lithium ion battery anodes: Influence of void spaces, shell and porous nanosheet. Electrochim. Acta *271*, 242–251. https://doi.org/10.1016/j.electacta.2018.03.144.
22. Xue, Y., Liu, J., Chen, H., Wang, R., Li, D., Qu, J., and Dai, L. (2012). Nitrogen-doped graphene foams as metal-free counter electrodes in high-performance dye-sensitized solar cells. Angew. Chem. Int. Ed. *51*, 12124–12127. https://doi.org/10.1002/anie.201207277.
23. Wu, C., Huang, X., Wu, X., Qian, R., and Jiang, P. (2013). Mechanically flexible and multifunctional polymer-based graphene foams for elastic conductors and oil-water separators. Adv. Mater. *25*, 5658–5662. https://doi.org/10.1002/adma.201302406.
24. Yang, C., Xu, Y., Man, P., Zhang, H., Huo, Y., Yang, C., Li, Z., Jiang, S., and Man, B. (2017). Formation of large-area stretchable 3D graphene–nickel particle foams and their sensor applications. RSC Adv. *7*, 35016–35026. https://doi.org/10.1039/c7ra05599d.
25. Huang, Z.-M., Zhang, Y.Z., Kotaki, M., and Ramakrishna, S. (2003). A review on polymer nanofibers by electrospinning and their applications in nanocomposites. Compos. Sci. Technol. *63*, 2223–2253. https://doi.org/10.1016/s0266-3538(03)00178-7.
26. Greiner, A., and Wendorff, J.H. (2007). Electrospinning: a fascinating method for the preparation of ultrathin fibers. Angew. Chem. Int. Ed. *46*, 5670–5703. https://doi.org/10.1002/anie.200604646.
27. Li, D., and Xia, Y. (2004). Electrospinning of nanofibers: Reinventing the wheel? Adv. Mater. *16*, 1151–1170. https://doi.org/10.1002/adma.200400719.
28. Dror, Y., Salalha, W., Khalfin, R.L., Cohen, Y., Yarin, A.L., and Zussman, E. (2003). Carbon nanotubes embedded in oriented polymer nanofibers by electrospinning. Langmuir *19*, 7012–7020. https://doi.org/10.1021/la034234i.
29. Hou, H., Ge, J.J., Zeng, J., Li, Q., Reneker, D.H., Greiner, A., and Cheng, S.Z.D. (2005).

Electrospun polyacrylonitrile nanofibers containing a high concentration of well-aligned multiwall carbon nanotubes. Chem. Mater. *17*, 967–973. https://doi.org/10.1021/cm0484955.

30. Ra, E.J., An, K.H., Kim, K.K., Jeong, S.Y., and Lee, Y.H. (2005). Anisotropic electrical conductivity of MWCNT/PAN nanofiber paper. Chem. Phys. Lett. *413*, 188–193. https://doi.org/10.1016/j.cplett.2005.07.061.
31. Svyntkivska, M., Makowski, T., Shkyliuk, I., and Piorkowska, E. (2023). Electrically conductive crystalline polylactide nonwovens obtained by electrospinning and modification with multiwall carbon nanotubes. Int. J. Biol. Macromol. *242*, 124730. https://doi.org/10.1016/j.ijbiomac.2023.124730.
32. Liu, X., Wang, C., Huang, Z., and Zhu, P. (2023). Electrospun multiwall nanotubes-loaded polyethylene glycol/polyacrylonitrile composite form-stable nanofibers for thermal energy storage. J. Energy Storage *66*, 107458. https://doi.org/10.1016/j.est.2023.107458.
33. Zhang, Y., Yang, S., Zhang, Q., Ma, Z., Guo, Y., Shi, M., Wu, H., and Guo, S. (2023). Constructing interconnected asymmetric conductive network in TPU fibrous film: Achieving low-reflection electromagnetic interference shielding and surperior thermal conductivity. Carbon *206*, 37–44. https://doi.org/10.1016/j.carbon.2023.01.043.
34. Flayeh, A.A., Kadhim, H.J., and Kareem, F.A. (2022). Role of polystyrene/multiwall carbon nanotubes concentrations on the morphological properties of prepared nanofibers nanocomposites. Fullerenes, Nanotub. Carbon Nanostruct. *31*, 136–146. https://doi.org/10.1080/1536383x.2022.2125960.
35. Miao, J., Miyauchi, M., Dordick, J.S., and Linhardt, R.J. (2012). Preparation and characterization of electrospun core sheath nanofibers from multi-walled carbon nanotubes and poly(vinyl pyrrolidone). J. Nanosci. Nanotechnol. *12*, 2387–2393. https://doi.org/10.1166/jnn.2012.5710.
36. Bao, Q., Zhang, H., Yang, J.-X., Wang, S., Tang, D.Y., Jose, R., Ramakrishna, S., Lim, C.T., and Loh, K.P. (2010). Graphene-polymer nanofiber membrane for ultrafast photonics. Adv. Funct. Mater. *20*, 782–791. https://doi.org/10.1002/adfm.200901658.
37. Li, Q., Yan, F., and Texter, J. (2020). Electrospinning graphene — Retention of anisotropy. MRS Adv. *5*, 2101–2110. https://doi.org/10.1557/adv.2020.263.
38. Lu, J., Yan, F., and Texter, J. (2009). Advanced applications of ionic liquids in polymer science. Prog. Polym. Sci. *34*, 431–448. https://doi.org/10.1016/j.progpolymsci.2008.12.001.
39. Qian, W., Texter, J., and Yan, F. (2017). Frontiers in poly(ionic liquid)s: Syntheses and applications. Chem. Soc. Rev. *46*, 1124–1159. https://doi.org/10.1039/c6cs00620e.
40. Li, Q., Yan, F., and Texter, J. (2024). Polymerized and colloidal ionic liquids — Syntheses and applications. Chem. Rev. *124*, 3813–3931. https://doi.org/10.1021/acs.chemrev.3c00429.
41. Yan, F., and Texter, J. (2006). Surfactant ionic liquid-based microemulsions for polymerization. Chem. Commun. *25*, 2696–2698. https://doi.org/10.1039/b605287h.
42. England, D., Tambe, N., and Texter, J. (2012). Stimuli-responsive nanolatexes: Porating films. ACS Macro Lett. *1*, 310–314. https://doi.org/10.1021/mz2002356.
43. England, D.; MS Thesis, Eastern Michigan University (2008). Materials and coatings derived from the polymerizable ionic liquid surfactant 1-(2-acryloyloxyundecyl)-3-methylimidazolium romide. https://commons.emich.edu/theses/159.
44. Yan, F., and Texter, J. (2010). Nanoporous and microporous solvogels and nanolatexes by microemulsion polymerization. US Patent 7,759,401, patent application 11/689,866. July 20, 2010.
45. Earle, M.J., Gordon, C.M., Plechkova, N.V., Seddon, K.R., and Welton, T. (2007). Decolorization of ionic liquids for spectroscopy. Anal. Chem. *79*, 758–764. https://doi.org/10.1021/ac061481t.
46. Page, K.A., England, D., and Texter, J. (2012). Capturing nanoscale structure in network gels by microemulsion polymerization. ACS Macro Lett. *1*, 1398–1402. https://doi.org/10.1021/mz300521d.
47. Texter, J., Ager, D., Vasantha, V.A., Crombez, R., England, D., Ma, X., Maniglia, R., and Tambe, N. (2012). Advanced nanocarbon materials facilitated by novel stimuli-responsive stabilizers. Chem. Lett. *41*, 1377–1379. https://doi.org/10.1246/cl.2012.1377.
48. Texter, J., Crombez, R., Maniglia, R., Ma, X., Arjunan Vasantha, V., Manuelian, M., Campbell, R., Slater, L., and Mourey, T. (2019). Imidazolium-based stabilization of aqueous multiwall carbon nanotube dispersions. J. Surf. Deterg. *22*, 1059–1071. https://doi.org/10.1002/jsde.12303.
49. Antonietti, M., Shen, Y., Nakanishi, T., Manuelian, M., Campbell, R., Gwee, L., Elabd, Y.A., Tambe, N., Crombez, R., and Texter, J. (2010). Single-wall carbon nanotube latexes. ACS Appl. Mater. Interfaces *2*, 649–653. https://doi.org/10.1021/am900936j.
50. Zhao, L., Crombez, R., Caballero, F.P., Antonietti, M., Texter, J., and Titirici, M.-M. (2010). Sustainable nitrogen-doped carbon latexes with high electrical and thermal conductivity. Polymer *51*, 4540–4546. https://doi.org/10.1016/j.polymer.2010.07.044.
51. Ager, D., Vasantha, V.A., Crombez, R., and Texter, J. (2014). Aqueous graphene dispersions — Optical properties and stimuli-responsive phase transfer. ACS Nano *8*, 11191–11205. https://doi.org/10.1021/nn502946f.
52. Texter, J. (2014). Nanoparticle dispersions with ionic liquid-based stabilizers. US patent 8,920,682. December 20, 2014.
53. Jacob, A. (2011). Bayer MaterialScience concludes nanotubes license agreement with Hyperion. https://www.reinforcedplastics.com/content/news/bayer-materialscience-concludes-nanotubes-license-agreement-with-hyperion/. accessed 25 January 2024.
54. Plastics-Today-Staff (2011). Big deal for tiny tubes: Bayer buys CNT license from Hyperion. https://www.plasticstoday.com/plastics-processing/big-deal-for-tiny-tubes-bayer-buys-cnt-license-from-hyperion. accessed 25 January 2024.
55. Meyer, H. (2008). Neuere Entwicklungen Neuere auf dem Gebiet der CNT - Herstellung und Nutzung im Faserverbundleichtbau. https://www.dlr.de/fa/Portaldata/17/Resources/dokumente/institut/wissenschaftstag_2008/Meyer.pdf. accessed 25 January 2024.
56. Cabane, B., and Duplessix, R. (1987). Decoration of semidilute polymer solutions with surfactant micelles. J. Phys. *48*, 651–662. https://doi.org/10.1051/jphys:01987004804065100.
57. Guyot, A., Audebert, R., Botet, R., Cabane, B., Lafuma, F., Jullien, R., Pefferkorn, E., Pichot, C., Revillon, A., and Varoqui, R. (1990). Floculation de particules colloïdales par les polymères hydrosolubles. J. Chim. Phys. *87*, 1859–1899. https://doi.org/10.1051/jcp/1990871859.
58. Mampallil, D., and Eral, H.B. (2018). A review on suppression and utilization of the coffee-ring effect. Adv. Colloid Interface Sci. *252*, 38–54. https://doi.org/10.1016/j.cis.2017.12.008.
59. Bigioni, T.P., Lin, X.M., Nguyen, T.T., Corwin, E.I., Witten, T.A., and Jaeger, H.M. (2006). Kinetically driven self assembly of highly ordered nanoparticle monolayers. Nat. Mater. *5*, 265–270. https://doi.org/10.1038/nmat1611.
60. Larson, R.G. (2014). Transport and deposition patterns in drying sessile droplets. AIChE J. *60*, 1538–1571. https://doi.org/10.1002/aic.14338.
61. Al-Milaji, K.N., and Zhao, H. (2019). New perspective of mitigating the coffee-ring effect: interfacial assembly. J. Phys. Chem. C *123*, 12029–12041. https://doi.org/10.1021/acs.jpcc.9b00797.
62. Velikov, K.P., Durst, F., and Velev, O.D. (1998). Direct observation of the dynamics of latex particles confined inside thinning water-air films. Langmuir *14*, 1148–1155. https://doi.org/10.1021/la970338f.
63. Kralchevsky, P.A., Denkov, N.D., Paunov, V.N., Velev, O.D., Ivanov, I.B., Yoshimura, H., and Nagayama:, K. (1994). Formation of two-dimensional colloid crystals in liquid films under the action of capillary forces. J. Phys. Condens. Matter *6*, A395–A402. https://doi.org/10.1088/0953-8984/6/23A/065.
64. Kralchevsky, P.A., and Denkov, N.D. (2001). Capillary forces and structuring in layers of colloid particles. Curr. Opin. Colloid Interface Sci. *6*, 383–401. https://doi.org/10.1016/S1359-0294(01)00105-4.
65. Texter, J., and Lelental, M. (1999). Network formation in nanoparticulate tin oxide-gelatin thin films. Langmuir *15*, 654–661. https://doi.org/10.1021/la980526l.
66. Texter, J. (2002). Dielectric spectroscopy of particle-based waterborne coatings. J. Non-Cryst. Solids *305*, 339–344. https://doi.org/10.10166/S0022-3093(02)01114-6.

STAR★METHODS

KEY RESOURCES TABLE

REAGENT or RESOURCE	SOURCE	IDENTIFIER
Chemicals, peptides, and recombinant proteins		
Acryloyl chloride	SigmaAldrich	Product #549797
Bromoundecanol	SigmaAldrich	Product #184136
Methyl imidazole	SigmaAldrich	Product #336092
Polyvinyl alcohol	Aladdin Chemical Reagent Company	https://www.china-pva.net/category/PVA-2488-PVA-2499.html
MWCNT - Baytubes®	Bayer MaterialScience	https://www.bayer04.de
Software and algorithms		
Origin 8.0 Pro	OriginLab	https://www.originlab.com/
CS ChemDraw Std	CambridgeSoft	Cole-Palmer Item # EW-82221-20;
Other		
Brookhaven 90Plus	Brookhaven Instruments	https://www.brookhaveninstruments.com/
Model QENZ-E05 electrospinning apparatus	Foshan Lepton Precision Measurement and Control Technology Co. Ltd., Foshan, China; now Foshan NanofiberLabs Co., Ltd.	https://www.qingzitech.com/about/10.html; https://www.nanofiberlabs.com/
Hitachi S-4700 scanning electron microscope	Hitachi High-Tech	https://www.hitachi-hightech.com/

RESOURCE AVAILABILITY

Lead contact

Subsequent inquiries and requests for materials and chemicals should be sent to and will be fulfilled by the lead contact, John Texter (jtexter@emich.edu).

Materials availability

No new reagents were created in this investigation.

Data and code availability

- On request, the lead contact will share the original data reported in this article.
- This article contains no original code.
- Any extra data necessary to reanalyze the data given in this research is accessible upon request from the lead contact.

METHOD DETAILS

Synthesis of ionic liquid acrylate monomer, ILBr

This nanolatex (NL) stabilizer is the primary material synthesized to effect the creation of the stable aqueous MWCNT dispersion used in our electrospinning processing. This NL is composed of an ionic liquid acrylate surfactant, ILBr, and methylmethacrylate (obtained commercially).

For the first step of ILBr synthesis,[41] 100 mmol (25.12 g) 11-bromoundecanol is dissolved in 100 ml THF in a three-neck 500 ml round bottom flask in an ice bath under nitrogen. Triethylamine (120 mmol, 12.14 g, 20% excess) is dissolved in 100 ml THF and is added to the stirred solution. Next, 120 mmol acryloyl chloride (9.7 ml, 20% excess) is added to 100 ml THF by syringe. This acryloyl chloride solution is then added dropwise to the stirred 11-bromoundecanol solution over a period of 30 min using an addition funnel. After addition of acryloyl chloride is completed, the ice bath is removed, and stirring is continued under a nitrogen atmosphere at room temperature for 48 hr. After 48 hours, the white salt precipitate is removed by filtration. The light yellow liquid filtrate is washed three times with 2% sodium bicarbonate in DI (deionized) water in a 500 ml separatory funnel. The washed filtrate is dried overnight over anhydrous magnesium sulfate. The resulting filtrate is then diluted with 100 ml methylene chloride and passed through a gravity column containing approximately 2 cm of neutral alumina. Solvents are removed by rotary evaporation at 45°C. The 11-bromoundecylacrylate structure is confirmed by ^{1}H NMR. ^{1}H NMR (400 MHz, $CDCl_3$, δ): 1.30 (m, 14H, -$CH_2(CH_2)_7CH_2$-), 1.65 (m, 2H, -$OCH_2CH_2(CH_2)_7$-), 1.85 (m, 2H, -$(CH_2)_7CH_2CH_2Br$), 3.40 (t, 2H, -CH_2CH_2Br), 4.10 (t, 2H, -$OCH_2CH_2(CH_2)_7$-), 5.80 (1H, CH_2=CH-), 6.10 (1H, CH_2=CH-), 6.40 (1H, CH_2=CH-).

For the second step, 11-bromoundecylacrylate is stirred with a 20% molar excess of 1-methylimidazole and 0.01% by weight 2,6-di-tert-butyl-4-methylphenol inhibitor at 40°C for 48 hr under a nitrogen atmosphere. After 48 hr, the viscous, amber liquid is washed three times with diethyl ether in a separatory funnel. The washed product is diluted with 100 ml of methylene chloride and is passed through a gravity column containing approximately 2 cm of neutral alumina. This filtered solution is placed in a Petri dish to allow evaporation of methylene chloride at room temperature. The resulting waxy-tan solid is dried under vacuum at room temperature, producing a white, powdery solid, ILBr. The ILBr structure is confirmed by ^{1}H NMR. ^{1}H NMR (400 MHz, $CDCl_3$, δ): 1.30 (m, 14H, -CH_2(CH_2)CH_2-), 1.65 (m, 2H, -OCH_2CH_2(CH_2)$_7$-), 1.85 (m, 2H, (CH_2)$_7CH_2CH_2$N-), 4.10 (m, 2H, -OCH_2CH_2(CH_2)$_7$-), 4.10 (m, 3H, -N-CH_3), 4.30 (t, 2H, -CH_2CH_2N-), 5.80 (1H, CH_2=CH-), 6.10 (1H, CH_2=CH-), 6.40 (1H, CH_2=CH-), 7.25 (d, 1H, -NCHCHN-), 7.35 (d, 1H, -NCHCHN-), 10.60 (s, -NCHN-).

During the second step above, alkyl scrambling[45,46] generates a small amount of N,N-bis(acryloylundecyl) imidazolium bromide side-product. The bis-functional monomer results in lightly crosslinked nanolatexes below.

Synthesis of nanolatex

A partial ternary phase diagram of this system is illustrated in Figure 1A,[42,43] where the composition for microemulsion polymerization we utilized is indicated by the pink "×" in the lower left corner. The microemulsion domain is a thermodynamically stable and somewhat exotic single-phase solution. Our nanolatexes are prepared by diluting 3.7 g of a stock solution of 60% ILBr (w/w) in MMA with 46.6 g of DI water to reach a total weight of 50 g (about 50 mL). AIBN initiator was present in the MMA stock solution at 0.5% (w/w) with respect to total monomer weight. The microemulsion solution is then heated to 60°C in a temperature-controlled oil bath and held overnight. The resulting suspension comprising about 55% (w/w) nanolatex, linear poly(ILBr-r-MMA), and a small amount of unpolymerized ILBr is used to produce aqueous MWCNT dispersions as illustrated in Figure 1B.

Structural properties

NMR (^{1}H NMR) measurements are done with JEOL 400 MHz NMR. The hydroxyundecyl acrylate and ILBr samples are prepared by dissolving about 15 mg of analyte in $CDCl_3$ in 5 mm OD NMR tubes. The nanolatexes are analyzed using a Brookhaven 90-Plus dynamic light scattering instrument. The number-frequency particle diameters are in the range of 20-30 nm.

SEM analysis of electrospun coatings are performed using a Hitachi S-3400N scanning electron microscope. All materials are sputter coated with gold on a Denton Vacuum Desk IV Cold Sputter/Etch unit to reduce surface charging by the electron beam.

Electrospinning

Electrospinning is done using a system that was obtained from Foshan Lepton Precision Measurement and Control Technology Co. Ltd. (model QENZ-E05, Foshan, China). A potential of about 20 kV is used to polarize the electrospinning suspension, and a 22-gauge-steel needle is mounted on a moveable assembly and the needle tip is placed about 10 cm away from an aluminum foil target fixed to a rotating mandrel. The aqueous MWCNT/NL-PVA suspension is fed to the needle by a 10 mL syringe pump at a flow rate of 0.6 mL h^{-1}. The needle is rastered back and forth over a distance of about 10 cm to produce a coating on the rotating target about 10 cm wide. The target and drum are rotated at about 400 revolutions per minute. The as-spun fibrous films were dried overnight in a vacuum at room temperature to remove weakly bound water.